AIAA 2016-1548

Simulation of a Hammerhead Payload Fairing in the Transonic Regime

Scott M. Murman and Laslo T. Diosady*

NASA Ames Research Center, Moffett Field, CA, USA

Abstract

Detached-eddy simulations of unsteady buffet in the transonic regime about a hammerhead payload fairing using the OVERFLOW solver are presented. The computed results are compared to mean and unsteady pressures measured by Coe and Nute. Details of the transonic flow physics provide understanding in regions where the simulation and experimental results mismatch. Spectral and proper orthogonal decompositions of the unsteady surface pressure field are presented to further aid the analysis. A sensitivity study for temporal resolution, spatial operator, and turbulence model is included.

1 Introduction

During ascent a rocket can experience low-frequency unsteady aerodynamic loading, typically referred to as "buffet", and usually associated with a flow separation. These loading oscillations are typically greatest in the transonic regime where shock interactions are present and typically the vehicle is near peak dynamic pressure. This buffet phenomenon is considered distinct from higher-frequency aeroacoustic excitations, though in many cases the

*Science and Technology Corporation

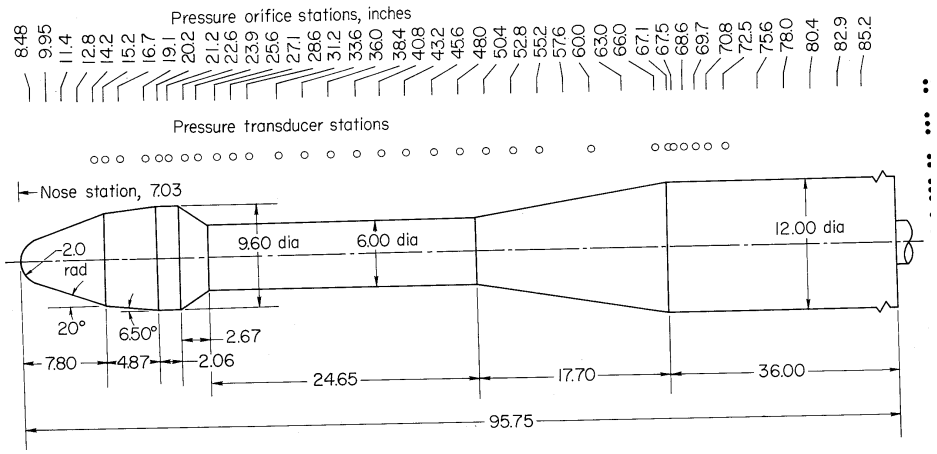

Figure 1: Model 11 hammerhead payload fairing geometry from Coe and Nute[1]. Units are in inches.

physics leading to both types of oscillations are similar. Given sufficient energy, the low-frequency buffet loads can resonate with lateral and longitudinal structural modes of the vehicle, with the potential for catastrophic failure.

There have been several experimental and numerical studies to better understand and predict buffet about launch vehicles in the transonic regime[1–7]. To date, these studies have predominately isolated the aerodynamic forcing using rigid models and applied this forcing as input to a separate structural model, *i.e.* decoupling the fluid-structure interaction to reduce the complexity of the analysis. Often the buffet phenomenon is effectively isolated around the payload fairing or nose cone, and the vehicle geometry can be simplified. The current work follows these prior simplifications, and considers a rigid model of an isolated forebody section with a "hammerhead" payload fairing, which is representative of the Atlas V, Delta II, Falcon 9, *etc.*

The current numerical study is part of a larger experimental program to document and analyze buffet using Coe and Nute's model 11 configuration[1](*cf.* Fig. 1). The current numerical results were used in pre-test model design and form a preliminary baseline for Computational Fluid Dynamics (CFD) predictions. The experimental results and comparison of CFD predictions against the new data will follow at a later date. Part of the motivation in re-visiting Coe and Nute's previous test is to develop a more complete validation dataset for CFD. In order for CFD to be a useful engineering tool in buffet analysis, confidence must be increased in the predictive capability, and the cost must be decreased. While a full solution to these issues is beyond the scope of the current work, this study does represent a step towards achieving these goals.

The current paper provides a detailed description of the physical mechanisms leading to buffet on the hammerhead configuration, as well as examining resolution requirements and hybrid-RANS turbulence model choices utilizing the OVERFLOW solver[8]. The comparisons against experimental data include mean static pressure measurements, and the root-mean-square (r.m.s.) oscillations of the pressure about the mean. The computed unsteady pressure loading on the vehicle is analyzed using both a spectral and proper-orthogonal decomposition. A small sensitivity study to the choice of numerical method and physical model is included.

2 Numerical Methods

The current work uses NASA's OVERFLOW solver, for structured overset grid topologies, which is representative of current "industrial" or "production" CFD technology. The feature-based adaption capability of OVERFLOW is used to generate a refined mesh at each specific flow condition[9]. A baseline mesh is generated which resolves the turbulent boundary layer, *i.e.* $y^+ \leq 1$ everywhere adjacent to the surface, and clusters near geometric features such as the changing slope of the conical fairing. An initial Cartesian off-body mesh is generated around these body-conforming grids based solely upon the geometry. From this baseline mesh both the body-conforming and Cartesian grids are adapted in a block Adaptive Mesh Refinement (AMR) manner. Figure 2 demonstrates this process from baseline to adapted mesh at typical transonic flow conditions. The final mesh is constrained to a maximum of 100M grid points. For comparison, the overset grid system for the entire Space Launch System (SLS) utilizes 375M grid points[10]. The baseline computations here use a constant timestep of $\Delta t = 2.0\text{x}10^{-5}$ sec. which is designed to resolve the oscillation of the flow separation behind the hammerhead fairing. A sensitivity study to temporal refinement is included in Sec. 4. The computed results all use the default 2nd-order central differencing with artificial dissipation scheme in OVERFLOW. Results using higher-order differencing to reduce the numerical dissipation are included in Sec. 4.

The unsteady separated flow is modeled using a hybrid-RANS approach. Following previous work by Brauckmann *et al.* [7], the Spalart-Allmaras turbulence model with modifications for Delayed Detached-Eddy Simulations (DDES) is utilized as the baseline. Sample results using the Shear-stress Transport (SST) model with DDES are included in Sec. 4.

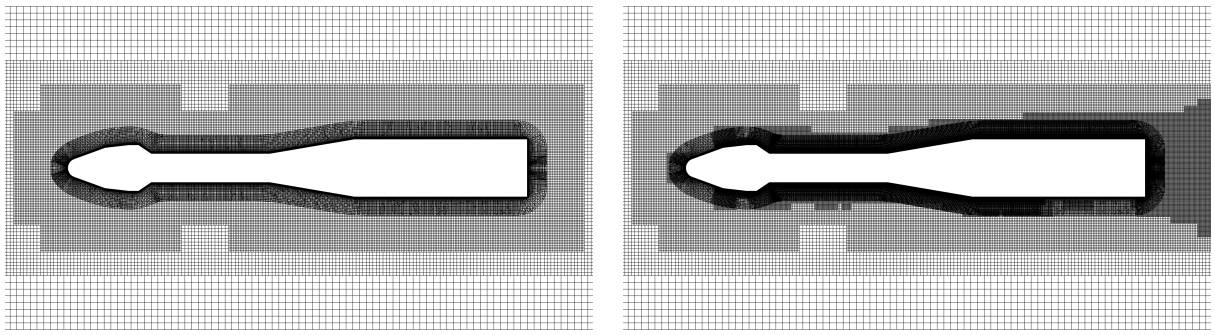

(a) Baseline **(b)** Adapted

Figure 2: Lateral symmetry plane for the Coe and Nute model 11 overset grid system.

3 Numerical Results

Coe and Nute's original experiment measured unsteady pressures on the model surface at several positions along the windward and lateral symmetry plane. Measurements were taken at $\alpha = 0°$, $4°$, and $8°$, and the Mach number was varied slightly about nominal design points to produce the most energetic pressure oscillations. The experimental Reynolds number (4M/foot) is roughly constant across the transonic range. The flow conditions for the computational simulations focus on $\alpha = 4°$ and several Mach numbers that are at, or close to, the experimental conditions.

The simulations were run through the initial unsteady transient, and then data was gathered for 0.5 sec. Pressure is sampled everywhere on the surface at 5000 Hz to mimic the sample rate for the upcoming unsteady pressure-sensitive paint (uPSP) experiment. Figure 3 presents a typical snapshot of the surface flowfield, and Fig. 4 contains contours of axial velocity along the lateral symmetry plane. The flow separates from the last change in slope on the conical payload fairing, and reattaches roughly 2/5 down the length of the cylindrical section. The time-averaged axial skin friction along the lateral symmetry plane along the fairing is presented in Fig. 5. The reversal of skin friction is aligned with the geometric change in slope, and remains fixed in time.

The flowfield in the recirculation region behind the payload fairing is unsteady and three-dimensional, with the reattachment location moving fore and aft, and the crossflow at angle of attack rotating the vorticity vectors. Downstream of the recirculation region the flow remains unsteady. Figure 6 presents a typical time history of the unsteady loading on the cylindrical section behind the payload fairing, and the same data converted to a histogram. While the data is not fully statistically converged, it is sufficient to capture mean and r.m.s. trends

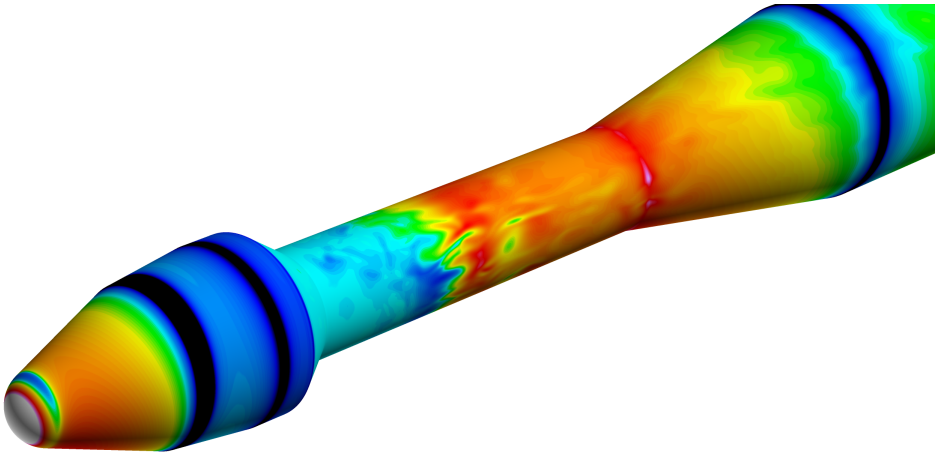

Figure 3: Computed surface pressure ($M_\infty = 0.8$, $\alpha = 4°$, $Re_D = 4\text{x}10^6$).

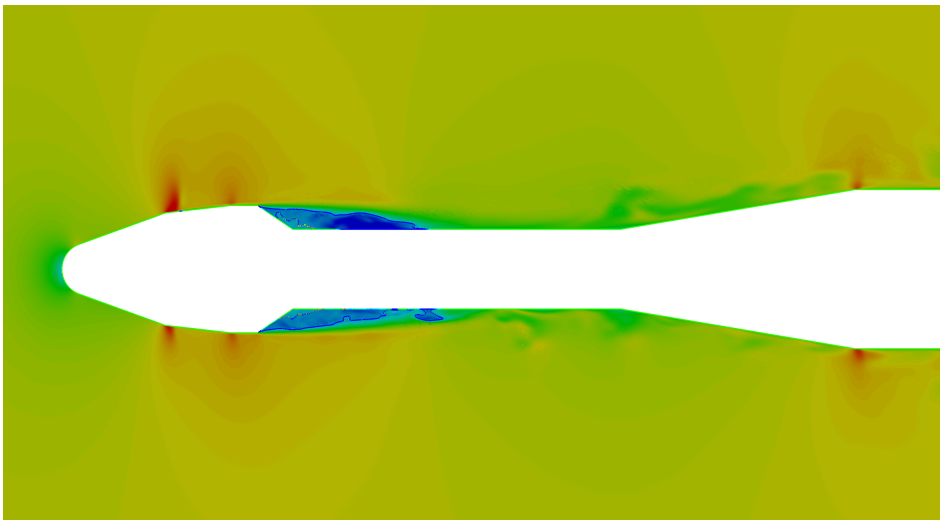

Figure 4: Color map of axial velocity along the lateral symmetry plane ($u \in [-0.3, 1.2]a_\infty$). The $u = 0$ contour line is highlighted. ($M_\infty = 0.8$, $\alpha = 4°$, $Re_D = 4\text{x}10^6$).

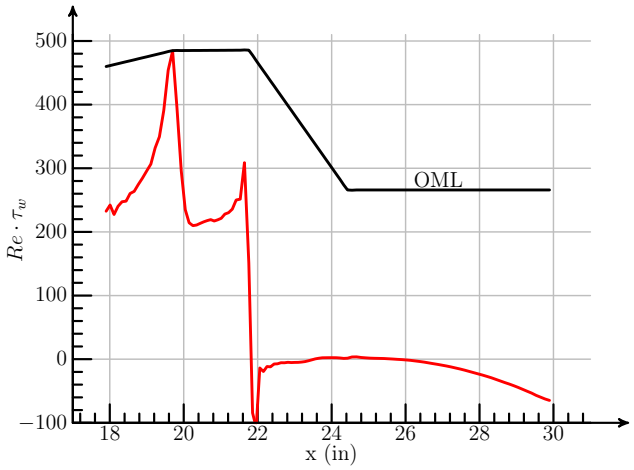

Figure 5: Time-averaged skin friction along the leeward lateral symmetry plane. ($M_\infty = 0.8$, $\alpha = 4°$, $Re_D = 4\text{x}10^6$).

for the preliminary analysis presented here. Each unsteady simulation requires roughly 50k cpu-hr on NASA's Pleiades supercomputer.

The mean pressure along the leeward and windward symmetry plane is compared against the experimental data at two Mach numbers in Fig. 7. In general, the agreement is good except for some discrepancies in the recirculation region behind the payload fairing, $20 \leq x \leq 40$ in. There appears to be a problem with the experimental data at Mach 0.95 for $x \leq 15$ in. Similar predictions of r.m.s. pressure fluctuations are presented in Fig. 8. The comparisons against experimental measurements for the fluctuations are not as good, with the CFD generally over-predicting the magnitude of the oscillation in the recirculation region, and predicting the peak too far downstream. There does not appear to be a clear trend with Mach number. The magnitude reduces at Mach 1.17, however the relative error is similar to the lower speed results. This behavior is consistent with the physical model underestimating the turbulent shear stress in the separated shear layer, which leads to overprediction of the size and extent of the recirculation region, as seen in simulations of 2D hump flow and flow over periodic hills[11, 12].

The CFD does pick up the peak in oscillations where the geometry changes slope, at $x = 50$ in. and $x = 68$ in., however the simulation results do not predict the sharp peak in oscillations on the payload chine near $x = 20$ in., most notably at Mach 0.8. This is expected due to the hybrid-RANS model approximations used in this region of shock-boundary layer interaction. The shock over the upstream chine thickens the boundary layer, increasing the turbulence intermittency in the outer region of the boundary layer (*cf.* Fig. 9).

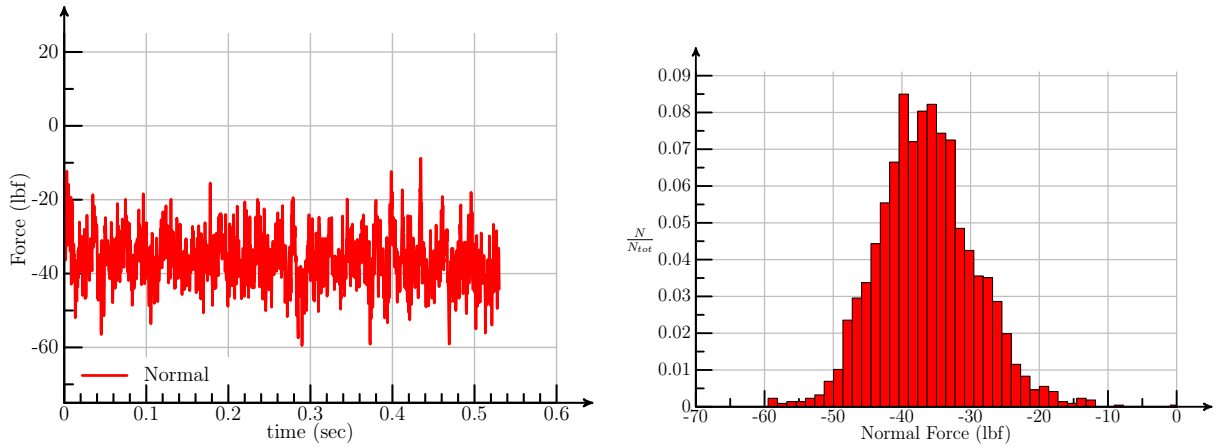

(a) Time-dependent **(b)** Histogram

Figure 6: Unsteady loading on the cylindrical section behind the payload fairing ($M_\infty = 0.8$, $\alpha = 4°$, $Re_D = 4\text{x}10^6$).

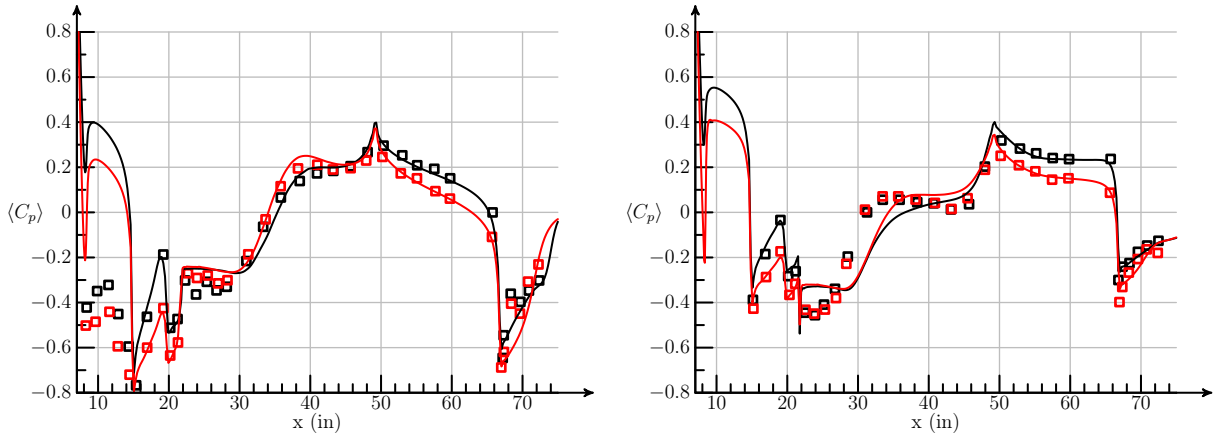

(a) $M_\infty = 0.95$ **(b)** $M_\infty = 1.17$

Figure 7: Computed mean pressure on the lateral symmetry plane compared to the experimental data of Coe and Nute[1]. Black is windward and red is leeward. ($\alpha = 4°$, $Re_D = 4\text{x}10^6$).

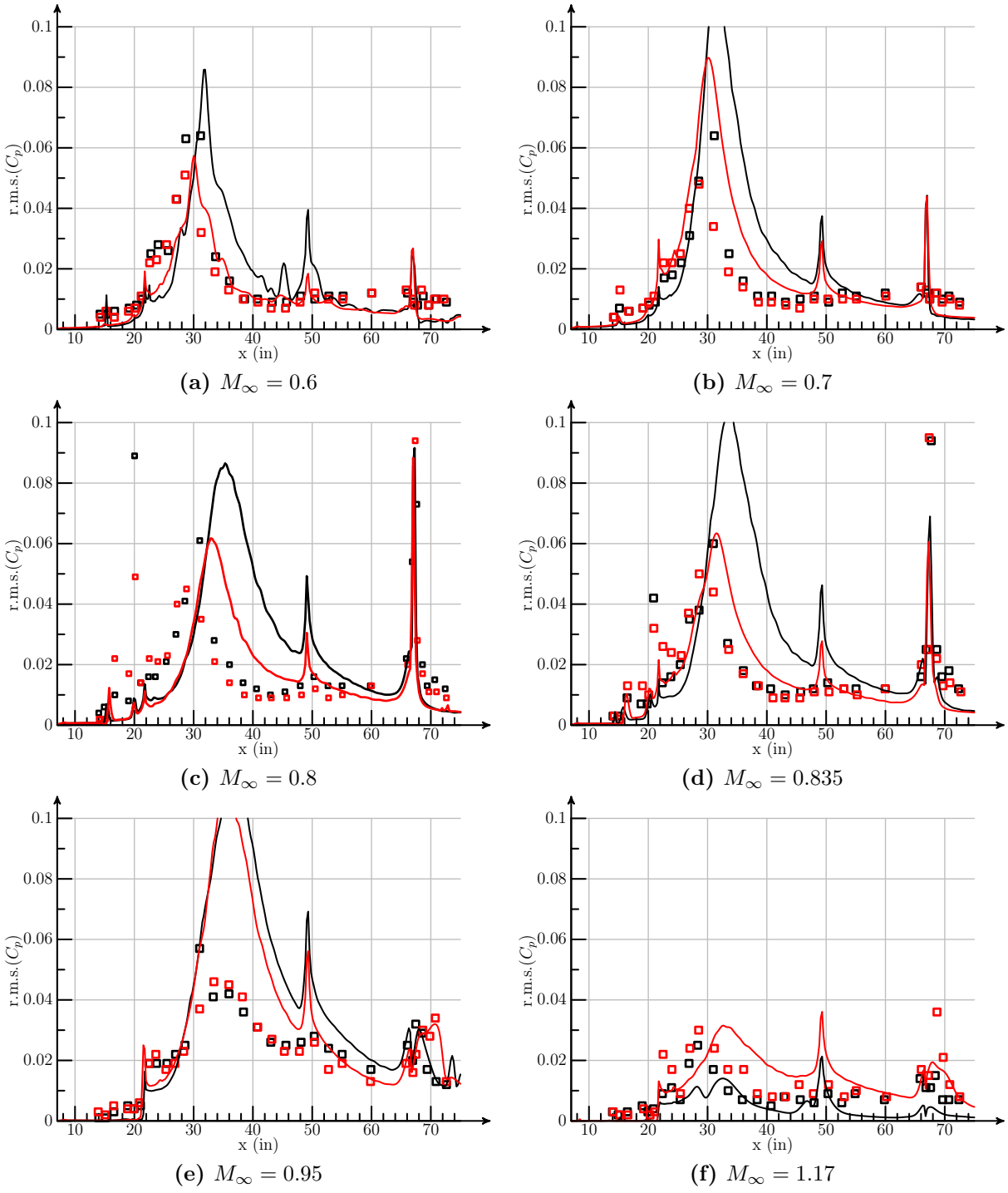

(a) $M_\infty = 0.6$ **(b)** $M_\infty = 0.7$

(c) $M_\infty = 0.8$ **(d)** $M_\infty = 0.835$

(e) $M_\infty = 0.95$ **(f)** $M_\infty = 1.17$

Figure 8: Computed r.m.s. pressure on the lateral symmetry plane compared to the experimental data of Coe and Nute[1]. Black is windward and red is leeward. ($\alpha = 4°$, $Re_D = 4\text{x}10^6$).

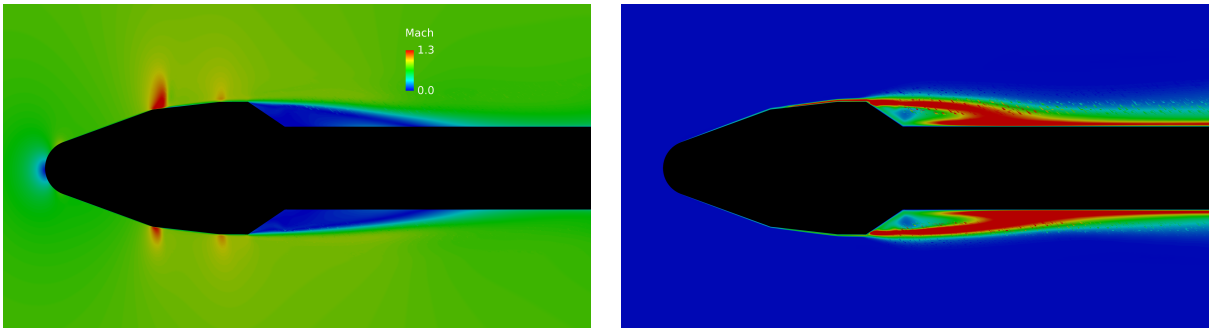

(a) Mach Number **(b)** Eddy Viscosity

Figure 9: Computed time-averaged contours in the lateral symmetry plane of the model. ($M_\infty = 0.8$, $\alpha = 4°$, $Re_D = 4\text{x}10^6$).

Above the second chine a supersonic "pocket" of flow is present. Physically, the turbulence intermittency at the edge of the boundary layer interacts with this supersonic region leading to very strong oscillations. The SA-DDES hybrid-RANS model treats the boundary layer as a RANS region, which is time-invariant, hence it cannot produce these same oscillations.

As well as looking at axial variations in r.m.s. pressure, the circumferential variation is examined at two locations on the cylindrical forebody section (Fig. 10). As expected, the growth in oscillations with downstream travel is symmetric at $\alpha = 0°$, however the influence of the crossflow rotation of the separated shear layer is observed at $\alpha = 4°$. As the crossflow merges on the leeward symmetry plane the oscillations are significantly damped.

3.1 Spectral and Proper-orthogonal Decomposition

For completeness, the mean and r.m.s. of the pressure on the surface is presented in Fig. 11. Due to the angle of attack, the flow reattaches further forward on the leeward section of the body than the windward, which is noticeable in the mean pressure. The r.m.s. of the oscillations show that the crossflow component of the flowfield generates the significant oscillations, whereas the legacy experimental data only measure the windward and leeward rays.

To aid in the analysis of buffet, the unsteady pressure oscillation is decomposed using a spectral approximation,

$$C_p(\boldsymbol{x}, t) - \langle C_p(\boldsymbol{x}, t) \rangle = \sum_k A_k(\boldsymbol{x}) e^{ikt} \tag{1}$$

The power spectral density (PSD) of the spectral decomposition at $x = 30$ in. along the

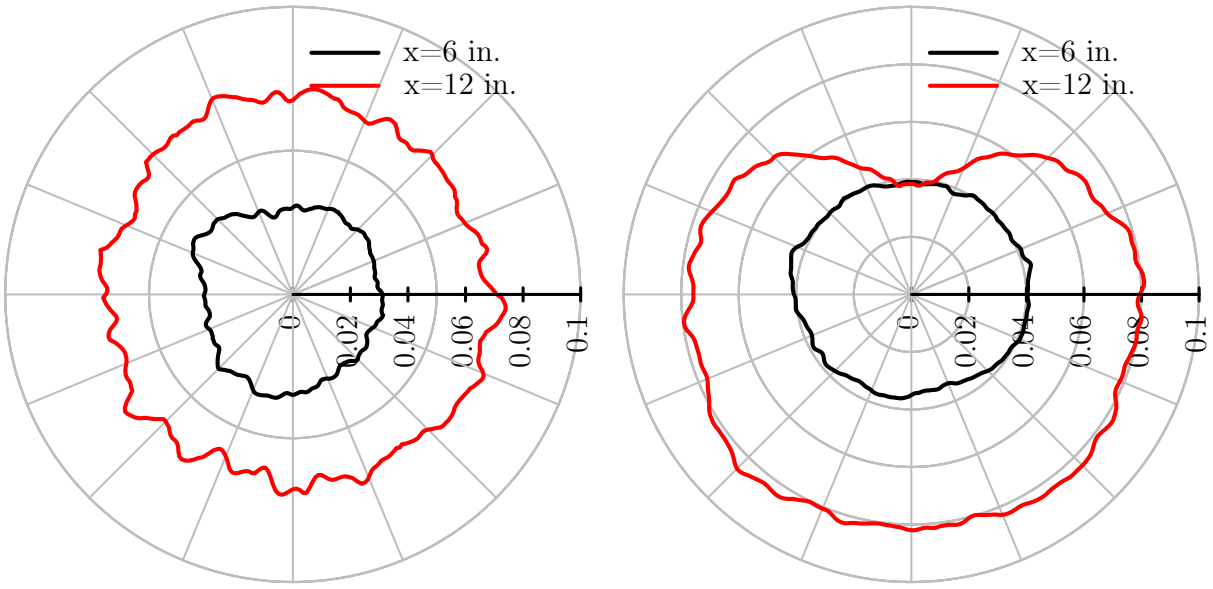

(a) $\alpha = 0°$ **(b)** $\alpha = 4°$

Figure 10: Computed r.m.s. pressure contours in axial planes 6 in. and 12 in. from the start of the model cylindrical section. ($M_\infty = 0.8$, $Re_D = 4\text{x}10^6$).

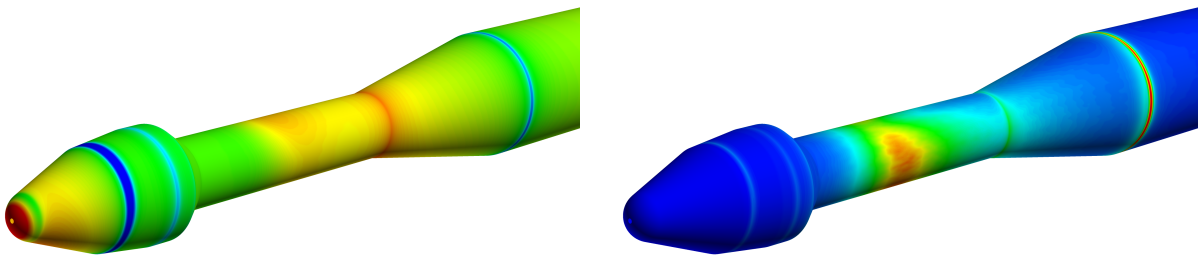

(a) Mean **(b)** r.m.s.

Figure 11: Computed mean and r.m.s. pressure on the model surface. ($M_\infty = 0.8$, $\alpha = 4°$, $Re_D = 4\text{x}10^6$).

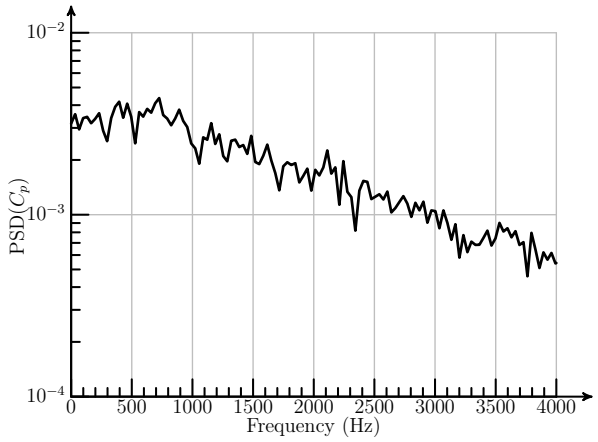

Figure 12: Power spectral density of pressure variation at $x = 30$ in. along the leeward lateral symmetry plane. ($M_\infty = 0.8$, $\alpha = 4°$, $Re_D = 4\text{x}10^6$).

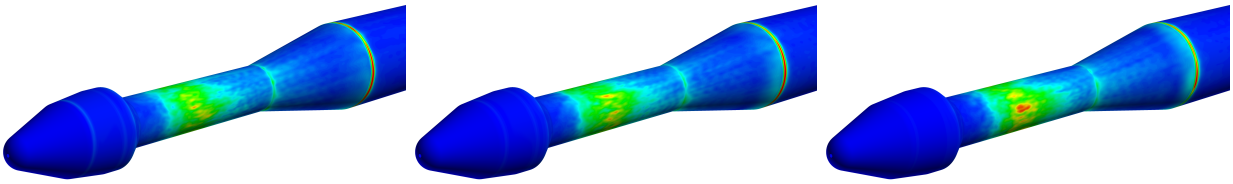

(a) 528 Hz **(b)** 726 Hz **(c)** 924 Hz

Figure 13: Magnitude of spectral decomposition of surface pressures. ($M_\infty = 0.8$, $\alpha = 4°$, $Re_D = 4\text{x}10^6$).

leeward lateral symmetry plane, roughly where the separated shear layer reattaches, is presented in Fig. 12. This PSD does not show a distinct frequency associated with the unsteady separation, and provides a more broad-spectrum response, which is consistent with the measurements of Coe and Nute[1]. The magnitude of the spectral coefficients on the surface, *i.e.* $|A_k(\boldsymbol{x})|$, are presented in Fig. 13 for three frequencies in the regime where most of the energy is contained. These show that roughly all of the energy is concentrated in the unsteady reattachment region, and that there is little difference between modes. The spectral decomposition does show a small increase in energy due to the crossflow.

An alternative to the spectral decomposition, which is somewhat complementary, is the proper-orthogonal decomposition (POD), also referred to as principal-component analysis, singular-value decomposition, Karhunen-Loève transform, *etc.*,

$$C_p(\boldsymbol{x}, t) - \langle C_p(\boldsymbol{x}, t) \rangle = \sum_k B_k(t) \lambda_k \phi_k(\boldsymbol{x}) \tag{2}$$

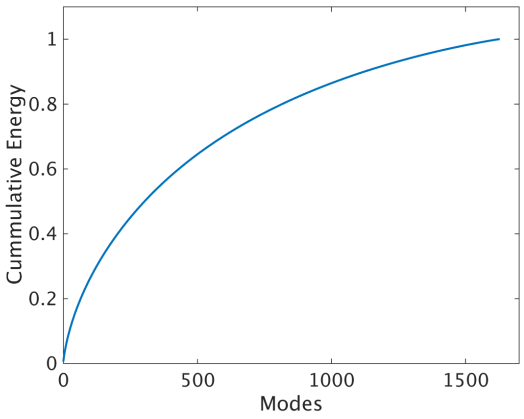

Figure 14: Cumulated energy in the POD of the surface pressure at $x = 30$ in. along the leeward lateral symmetry plane. ($M_\infty = 0.8$, $\alpha = 4°$, $Re_D = 4\text{x}10^6$).

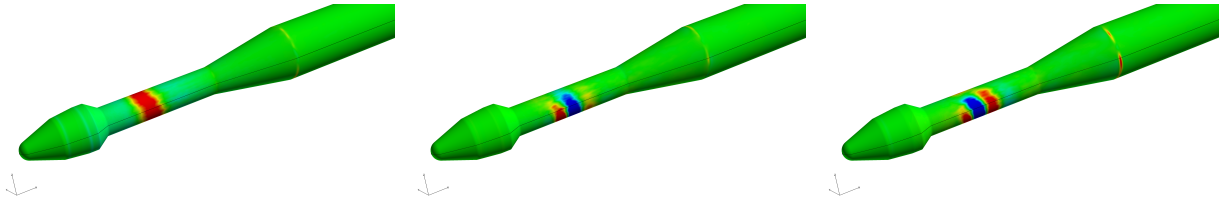

(a) Mode 1 **(b)** Mode 2 **(c)** Mode 3

Figure 15: POD modes of the surface pressure. ($M_\infty = 0.8$, $\alpha = 4°$, $Re_D = 4\text{x}10^6$).

The cumulative energy of the POD modes is presented in Fig. 14. As the POD ranks the modes from greatest to least energy, this clearly shows a broad-spectrum response as well, as it requires hundreds of modes to accumulate even half of the energy. The shape of POD modes 1, 2, and 3, *i.e.* $\phi_k(\boldsymbol{x})$, is presented in Fig. 15. The first mode corresponds to the fore and aft movement of the reattachment on the cylindrical section. Modes 2 and 3 show a periodic oscillation in the axial direction which superimposes upon the first mode.

4 Sensitivity Analysis

A limited sensitivity analysis to timestep, numerical scheme and turbulence model was performed. As with the above discussion, the results focus on the $M_\infty = 0.8$, $\alpha = 4°$ conditions as representative, and only the r.m.s. pressure oscillations are discussed. In all cases the change in mean flow from the baseline simulations discussed above is negligible.

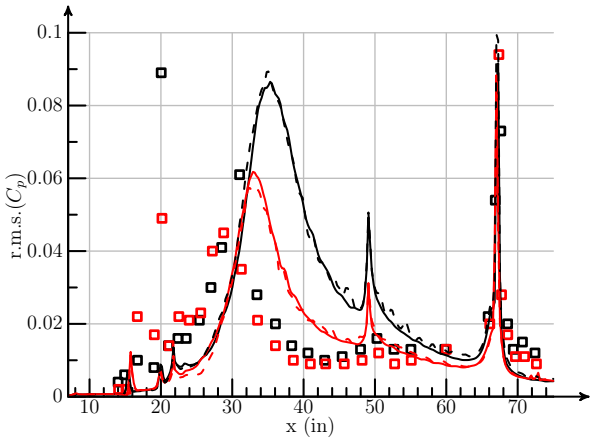

Figure 16: Computed r.m.s. pressure on the lateral symmetry plane compared to the experimental data of Coe and Nute[1]. Black is windward and red is leeward. Solid lines $\Delta t = 2\text{x}10^{-5}$ sec, dashed lines $\Delta t = 4\text{x}10^{-6}$ sec ($M_\infty = 0.8$, $\alpha = 4°$, $Re_D = 4\text{x}10^6$).

First, the timestep was reduced by a factor of 1/5 and the simulations run for the same amount of physical time for statistical sampling. The computed r.m.s. pressure demonstrates that the changes in surface pressure with increasing time resolution are negligible (Fig. 16).

For this preliminary study a grid refinement study beyond the current resolution was deemed computationally too expensive. To assess the sensitivity to reduced numerical dissipation associated with the spatial operators, high-order central-differencing options for the inviscid terms in OVERFLOW were utilized, namely 4th-order and 6th-order (FSO3 and FSO5 respectively in OVERFLOW namelist). These options have demonstrated improvements in predicting rotorcraft tip vortices, while still maintaining robustness[13]. In the current work, the higher-order operators increased the r.m.s. pressure on the windward side, further decreasing the fidelity of the comparisons against the experimental data (Fig. 17). The changes on the leeward side are smaller, and inconclusive.

These above sensitivity tests indicate that physical modeling deficiencies may be the dominate cause of the mis-prediction of the unsteady loadings in the recirculation region, even though the primary separation location is essentially fixed. To examine this, simulations were performed using the SST-DDES model. The computed results in Fig. 18 indicate the SST-DDES results further increase the r.m.s. pressure beyond the experimental results.

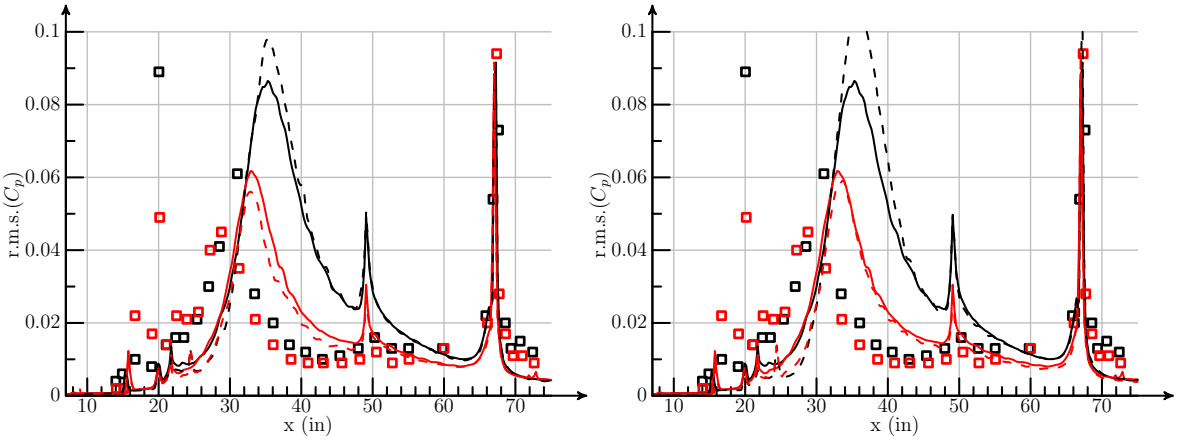

(a) 4th-order **(b)** 6th-order

Figure 17: Computed r.m.s. pressure on the lateral symmetry plane compared to the experimental data of Coe and Nute[1]. Black is windward and red is leeward. Solid lines 2nd-order inviscid operator, dashed lines higher-order operator ($M_\infty = 0.8$, $\alpha = 4°$, $Re_D = 4\text{x}10^6$).

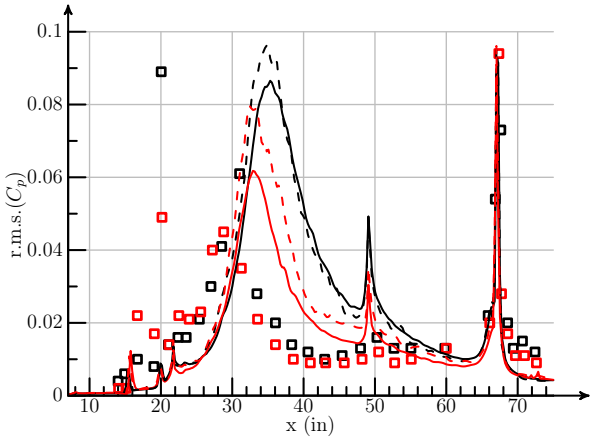

Figure 18: Computed r.m.s. pressure on the lateral symmetry plane compared to the experimental data of Coe and Nute[1]. Black is windward and red is leeward. Solid lines SA, dashed lines SST ($M_\infty = 0.8$, $\alpha = 4°$, $Re_D = 4\text{x}10^6$).

5 Summary

Detached-eddy simulations of transonic buffet for the Coe and Nute experimental geometry were performed as part of an analysis to prepare for a new experiment using this configuration, and to provide a baseline for CFD predictions using current production methods. While the predictions of mean pressure are relatively good, the CFD predictions of the unsteady pressure oscillations are consistently too large in magnitude, and indicate the extent of the recirculation region behind the payload fairing is larger than the experimental data indicates. While it cannot be ruled out that a lack of sufficient resolution is the cause of the discrepancies, the limited sensitivity studies undertaken to date indicate that physical model limitations may be the dominant factor.

While the primary separation location is fixed by geometry for this configuration, details of the modeling approach upstream of the separation are still seen to have an impact on the fidelity of the unsteady predictions. Specifically, the DES hybrid-RANS approach utilized here cannot account for intermittency in the attached boundary layer upstream of the separation. This intermittency interacts with the high-speed flow over the payload fairing causing an exchange of acoustic energy which is not accounted for in the DES simulations. The overprediction of the extent of the recirculation region also points to potential modeling deficiencies for the separated shear layer itself. Commonly RANS, and RANS-derived models, underpredict the turbulent shear stress in the separated shear layer, and the current results are consistent with this possibility.

The updated experimental data will include more detailed measurements to aid the improvement of CFD simulations. Surface pressure will be available across the entire body using the uPSP technique, and a limited off-body visualization using a shadowgraph technique will also be gathered. Given the current results, a desirable next step if to apply a true large-eddy simulation (LES) method, which is theoretically capable of capturing the boundary layer interaction and providing accurate predictions of separated shear layers, to this configuration and compare against the updated high-resolution data and current benchmark CFD predictions.

References

[1] Coe, C.F. and Nute, J.B., "Steady and Fluctuating Pressures at Transonic Speeds on Hammerhead Launch Vehicles," NASA TM X-778, 1962.

[2] Coe, C.F. and Kaskey, A.J., "The Effects of Nose Bluntness on the Pressure Fluctuations Measure on 15° and 20° Cone-Cylinders at Transonic Speeds," NASA TM X-779, 1963.

[3] Engblom, W.A., "Numerical Simulation of Titan IVB Transonic Buffet Environment," *Journal of Spacecraft and Rockets*, vol. 40, no. 5, pp. 648–656, 2003.

[4] Dotson, K.W. and Engblom, W.A., "Vortex-induced vibration of a heavy-lift launch vehicle during transonic flight," *Journal of Fluids and Structures*, vol. 19, no. 5, pp. 669–680, 2004.

[5] Piatak, D.J., Sekula, M.K., and Rausch, R.D., "Ares Launch Vehicle Transonic Buffet Testing and Analysis Techniques," *Journal of Spacecraft and Rockets*, vol. 49, no. 5, pp. 798–807, 2012.

[6] Tsutsumi, S., Takaki, R., Takama, Y., Imagawa, K., Nakakita, K., and Kato, H., "Hybrid LES/RANS Simulations of Transonic Flowfield around a Rocket Fairing," AIAA Paper 2012-2900, 2012.

[7] Brauckmann, G.J., Streett, C.L., Kleb, W.L., Alter, S.J., Murphy, K.J., and Glass, C.E., "Computational and Experimental Unsteady Pressures for Alternate SLS Booster Nose Shapes," AIAA Paper 2015-0559, 2015.

[8] Nichols, R.H., Tramel, R.W., and Buning, P.G., "Solver and Turbulence Model Upgrades to OVERFLOW 2 for Unsteady and High-Speed Applications," AIAA Paper 2006-2824, 2006.

[9] Buning, P.G. and Pulliam, T.H., "Cartesian Off-body Grid Adaptation for Viscous Time-Accurate Flow Simulation," AIAA Paper 2011-3693, 2011.

[10] Rogers, S.E., Dalle, D.J., and Chan, W.M., "CFD Simulations of the Space Launch System Ascent Aerodynamics and Booster Separation," AIAA Paper 2015-0778, 2015.

[11] Rumsey, C.L., Gatski, T.B., Sellers, W.L., Vatsa, V.N., and Viken, S.A., "Summary of the 2004 Computational Fluid Dynamics Validation Workshop on Synthetic Jets," *AIAA Journal*, vol. 44, no. 2, pp. 194–207, 2006.

[12] Murman, S.M., "A Scalar Anisotropy Model for Turbulent Eddy Viscosity," *International Journal of Heat and Fluid Flow*, vol. 42, pp. 115–130, August 2013.

[13] Chaderjian, N.M. and Ahmad, J.U., "Detached Eddy Simulation of the UH-60 Rotor Wake Using Adaptive Mesh Refinement," in *AHS International Forum*, 2012.